ACS SENSORS

pubs.acs.org/acssensors

Article

DNA-Engineered $CsPbBr_3$ Superlattices with Enhanced Electronic Coupling for High-Performance Electrochemiluminescence Biosensing

Yongli Wu, Zhuoxin Ye, Yuxuan Chen, Yan Zhang, Ruiyan Liu, Pinyi Ma,* and Daqian Song*

Cite This: *ACS Sens.* 2025, 10, 6231−6240

Read Online

ACCESS | Metrics & More | Article Recommendations | Supporting Information

ABSTRACT: Perovskite quantum dots (PQDs), particularly $CsPbBr_3$ QDs, are highly promising electrochemiluminescent (ECL) materials due to their excellent optical properties. However, the key challenge in developing PQD materials for practical applications lies in balancing the contradiction between their intrinsic instability in aqueous environments and ECL efficiency. To address this challenge, we employed DNA nanosheets as templates to direct the self-assembly of $CsPbBr_3$ QDs, into highly ordered two-dimensional superlattices. This strategy enhances electronic coupling effects through long-range ordered arrangement, enabling rapid charge-carrier transport. High-resolution XPS confirmed charge transfer between $CsPbBr_3$ QDs, while AFM characterization reveals that the nanosheets possess a periodic structure with a spacing of 63.4 nm. Compared to unassembled $CsPbBr_3$ QDs, the ECL intensity of $CsPbBr_3$/DNA NSs increased by 2.5-fold, with a respectably high ECL efficiency of 65.5%. Remarkably, they retain 83.3% of the initial ECL intensity retained after 10 days in aqueous conditions, significantly surpassing the stability of unprotected $CsPbBr_3$. Furthermore, these nanosheets were successfully applied in a ratiometric ECL biosensor for miRNA-221 detection, achieving a detection limit of 6.05 aM. This study presents a novel strategy that simultaneously addresses the aqueous instability and enhances the ECL efficiency of $CsPbBr_3$ QDs, significantly advancing their applications in biosensing.

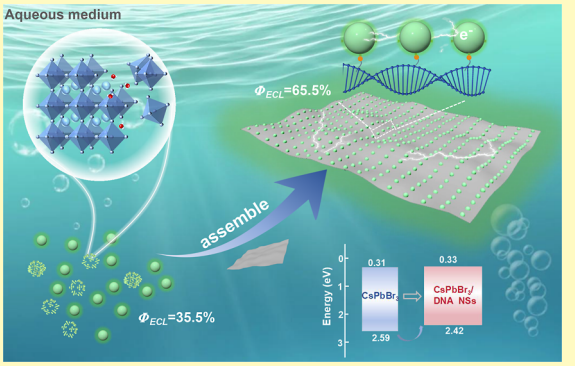

KEYWORDS: *DNA nanosheets, $CsPbBr_3$ QDs, self-assembly, electrochemiluminescence, aqueous environment, ECL efficiency*

$CsPbBr_3$ quantum dots (QDs) have emerged as highly promising electrochemiluminescent (ECL) materials due to their outstanding optical properties, including high photoluminescence quantum yield,[1] broad excitation spectra, narrow emission bands, and tunable emission across the visible spectrum,[2] These attributes make PQDs suitable for a range of optoelectronic applications,[3,4] positioning them as one of the most attractive materials for use in ECL-based biosensors. However, the inherent instability of PQDs, especially in aqueous and high-humidity environments, severely limits their practical use in biodetection and other sensing applications.[5,6] Therefore, enhancing the water resistance of PQDs while maintaining their ECL efficiency is critical for expanding their applications in these fields.

Current strategies to improve PQDs stability primarily focus on two approaches: surface modification through ligand substitution[7] and encapsulation with inorganic oxides or polymers.[8,9] The protective matrices can isolate PQDs from the external environment to enhance their stability. There are relatively few studies on PQDs for sensing applications in aqueous media, and Tan[10] was the first to investigate the redox and electrochemiluminescence properties of halide perovskite $CH_3NH_3PbBr_3$ NCs in aqueous medium. Therefore, the redox and charge transfer properties of PQDs in aqueous media remain poorly understood and warrant further investigation.

Nanomaterial morphology control is crucial for enhancing performance in electro-optical applications. Two-dimensional (2D) nanomaterials, in particular, offer significant advantages due to their large surface areas and strong quantum confinement effects.[11] Research indicates have shown that 2D perovskite films exhibit significantly improved stability in both air and water.[12] However, PQDs, which exhibit impressive self-assembly capabilities into diverse superstructures like nanowires,[13,14] nanosheets,[15−17] and nanocubes,[18] are unfortunately only stable in organic solvents. This presents a significant hurdle for their application in biosensing, where stable, well-ordered structures are essential for reliable performance in aqueous media.

Received: June 10, 2025
Revised: July 10, 2025
Accepted: July 25, 2025
Published: July 31, 2025

https://doi.org/10.1021/acssensors.5c02005
ACS Sens. 2025, 10, 6231−6240

Scheme 1. Schematic Illustration of the Formation of High—Order Nanostructures Assisted by Templates: (a) The $CsPbBr_3$/DNA NSs; (b) Conjugation of $CsPbBr_3$ QDs with Streptavidin

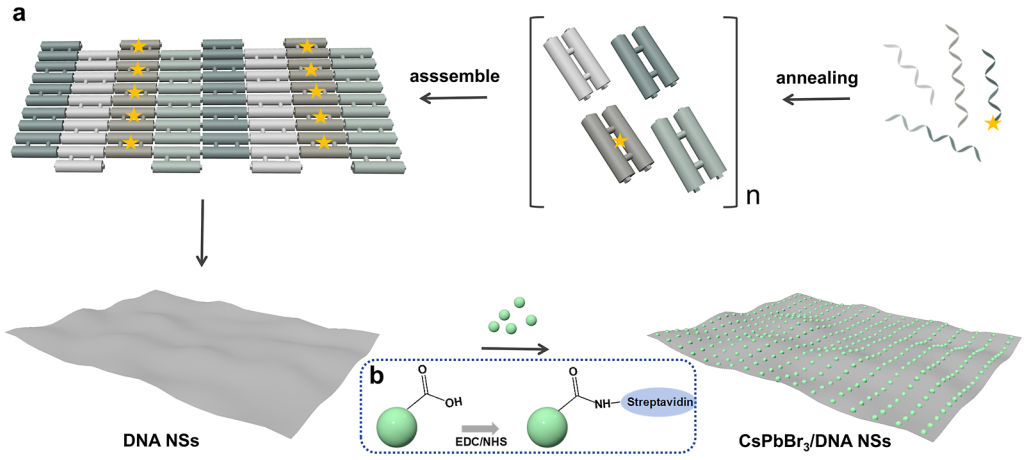

DNA nanotechnology offers a highly promising solution to address this challenge. DNA molecules possess inherent self-assembly capabilities and well-defined spatial conformations, making them ideal scaffolds for constructing structurally precise nanomaterials.[19] Close-packed QD solids not only retain the energy-level tunability conferred by quantum confinement effects but also exhibit exceptional charge transport properties due to significantly enhanced interdot electronic coupling.[20−22] With advancements in DNA nanotechnology, researchers can now precisely design DNA template structures spanning the nanoscale to microscale. By achieving accurate control over inter-QD spacing, this approach effectively promotes short-range charge transfer between QDs,[23] thereby opening new avenues for resolving the performance challenges of perovskite QDs in aqueous environments.

In this study, we innovatively employ DNA nanosheets as molecular templates to precisely guide the self-assembly of $CsPbBr_3$ QDs into superlattice structures with high ordering and dense packing characteristics. The synergistic interactions between QDs effectively enhance electronic coupling and band alignment, leading to significantly improved ECL performance with the efficiency increasing from 33.5% to 65.5%. Moreover, this architecture effectively prevents NC aggregation, maintaining 83.3% of the initial ECL intensity after 10 days of storage in aqueous environment. These advancements establish $CsPbBr_3$/DNA nanosheets (NSs) as a highly promising stable and efficient ECL nanoluminophore. Building on these findings, we further developed a ratiometric ECL detection strategy by constructing an ECL-resonance energy transfer (ECL-RET) system. This dual-potential ECL biosensor utilizes $CsPbBr_3$/DNA NSs as the ECL donor and platinum nanoparticle-luminol as the ECL acceptor. Based on measuring the ratio of two ECL signals, enables highly selective and sensitive detection of target microRNA, significantly improving the accuracy and reliability of the biosensor. This work provides novel research concepts and technical pathways for developing advanced ECL material systems with high stability and efficiency.

EXPERIMENTAL SECTION

Assembly of DNA Nanosheets. All DNA strands were purchased from Shanghai and purified using denaturing PAGE, except for the biotin-labeled DNA strands, which were purified using HPLC. The DNA nanosheets (DNA NSs) were assembled by mixing equimolar quantities of all constituent strands at a concentration of 2 μM in 1× TAE-Mg^{2+} buffer (40 mM Tris, 20 mM acetic acid and 12.5 mM magnesium acetate, pH 8.0). The mixture was gradually cooled from 90 °C to room temperature to allow proper assembly.

Synthesis of $CsPbBr_3$/DNA NSs. The SA-$CsPbBr_3$ QDs solution was mixed with the DNA NSs solution at a volume ratio of 1:10. The mixture was ultrasonicated for 30 min at 37 °C to obtain $CsPbBr_3$/DNA NSs. The same procedure was performed without adding $CsPbBr_3$ QDs as a control.

Preparation of the ECL-RET Biosensor. To prepare the ECL-RET biosensor, a glassy carbon electrode (GCE) (diameter: 3 mm) was polished with alumina particles of 0.3 and 0.05 μm. The electrode was washed with 50% ethanol, 0.5 M H_2SO_4, and ultrapure water, then dried under pure nitrogen gas. Afterward, 10 μL of $CsPbBr_3$/DNA NSs was uniformly deposited onto the GCE (labeled as $CsPbBr_3$/DNA NSs/GCE) and dried in an oven at 37 °C for 1 h. Next, 10 μL of the Assist DNA solution was added to the $CsPbBr_3$/DNA NSs/GCE (labeled as Assist DNA/$CsPbBr_3$/DNA NSs/GCE) and incubated for 1 h at 37 °C. The electrode was then rinsed with 10 mM potassium phosphate buffer (pH 7.4) to remove any unattached probe molecules.

RESULTS AND DISCUSSION

Synthesis and Characterization of $CsPbBr_3$/DNA Nanosheets (NSs). High loadings have been demonstrated to enhance structural stability,[24] making them suitable for meeting the demands of highperformance PQDbased photoelectric applications.[25,26] With the aim of enhancing the performance of $CsPbBr_3$ QDs in aqueous environments, this study utilizes the addressability of DNA nanosheets to fabricate structurally stable and closely packed $CsPbBr_3$ QDs. Scheme 1a illustrates the fabrication process of $CsPbBr_3$ QDs assembled on DNA nanosheets (NSs). To achieve this, four different double-crossover DNA "tiles" were employed as scaffolds (Figures S1 and S2), which spontaneously self-assemble into a regular two-dimensional (2D) structure. The design of these tiles follows an approach reported earlier,[27] with modifications: the A-tile features short DNA stems and biotin protruding from the plane of the tile, while the remaining tiles (B, C and D) determine a precise spatial separation of 64 nm between the rows of the A components. This spatial arrangement results in DNA nanosheets with regularly spaced biotin binding sites, which are used to control the location of streptavidin-conjugated perovskites. Capitalizing on streptavidin's tetrameric structure, each SA-PQD

https://doi.org/10.1021/acssensors.5c02005
ACS Sens. 2025, 10, 6231−6240

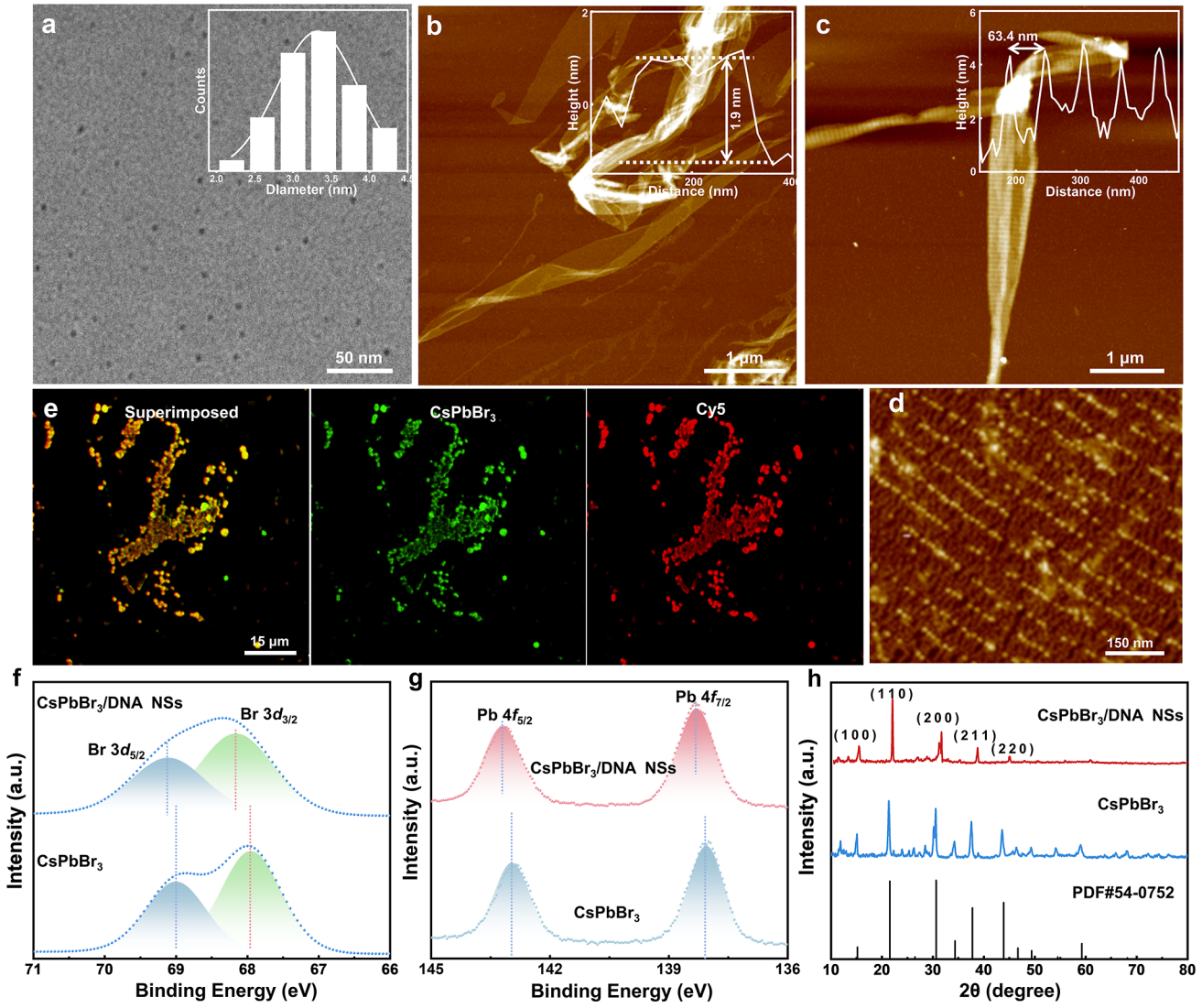

Figure 1. Material synthesis and characterization of morphology. (a) TEM of SA-$CsPbBr_3$ and size distribution of SA-$CsPbBr_3$ QDs, (b) AFM images of the DNA nanosheets with each A tile bearing a biotin, (c) the biotinylated DNA nanosheets incubated with SA-$CsPbBr_3$ QDs conjugate and the cross-section analysis of the AFM images. (d) The AFM high magnification and (e) confocal fluorescence microscopyimages of $CsPbBr_3$/DNA NSs. High resolution XPS spectra of $CsPbBr_3$ QDs and $CsPbBr_3$/DNA NSs. (f) Br, (g) Pb, (h) XRD patterns of SA-$CsPbBr_3$ QDs and $CsPbBr_3$/DNA NSs.

establishes multivalent interactions with multiple biotin moieties on the DNA scaffold. This high-fidelity biomolecular recognition system achieves site-specific QD immobilization while effectively suppressing nonspecific aggregation, ultimately producing two-dimensional superlattice whose periodicity is precisely programmed by the underlying DNA template.

The size and morphology of the $CsPbBr_3$ QDs were characterized using transmission electron microscopy (TEM). The QDs, synthesized via ligand-assisted reprecipitation (LARP),[28] were found to be uniform and monodisperse, with a particle size distribution of 3.5 ± 1.4 nm (Figure 1a). The $CsPbBr_3$ QDs demonstrate exceptional optoelectronic properties, exhibiting bright narrow band green photoluminescence centered at 516 nm with an 18 nm full width at half-maximum (fwhm) and an obvious absorption peak at 508 nm (Figure S3). Atomic force microscopy (AFM) further demonstrated that the biotin-labeled DNA nanosheets were smooth, with the height profiles indicating that the thickness of the nanosheets at the initial assembly stage was approximately 1.8 nm (Figure 1b). Upon adding SA-$CsPbBr_3$ QDs to the DNA scaffold solution, AFM images (Figures 1c,d and S4) showed that the QDs were arranged into a long-range ordered close-packed superlattice, confirming the specific binding of the SA-$CsPbBr_3$ QDs to the DNA nanosheets and the 2D structures have a dimension of micrometer size. The cross-sectional AFM profiles (Figure 1c inset) revealed that the average height increased by approximately 4 nm compared to the unfunctionalized nanosheets, indicating the successful integration of the QDs into the DNA nanosheet structure. Additionally, the observed periodicity of five peaks with a spacing of 63.4 nm closely matched the expected 64 nm, further verifying the regularity of the self-assembled structure. A controlled experiment using streptavidin added to biotin-modified DNA nanosheets showed a height change of only 1.25 nm (Figure S5), AFM measurements of streptavidin under different forces (30 pN, 60 pN, and 110 pN) revealed a maximum height reduction to 1.15, 0.65, and 0.25 nm,

https://doi.org/10.1021/acssensors.5c02005
ACS Sens. 2025, 10, 6231−6240

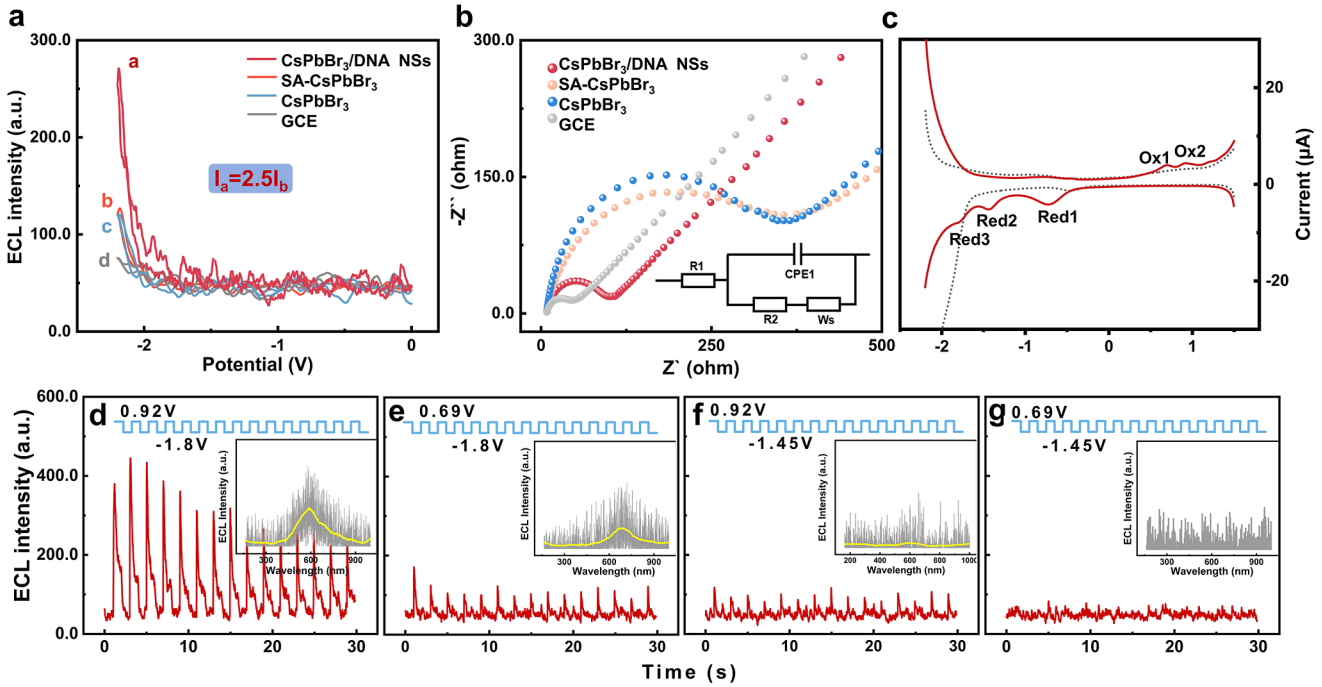

Figure 2. (a) ECL-potential curves of bare GCE, $CsPbBr_3$ and $CsPbBr_3$/DNA NSs in 0.01 M PBS (pH = 7.4), (b) EIS of $CsPbBr_3$ and $CsPbBr_3$/DNA NSs in the 5 mM $[Fe(CN)_6]^{3-/4-}$ solutio, (c) DPV curves of GCE in 0.01 M N_2-saturated PBS (pH = 7.4), transient ECL (red curves) of $CsPbBr_3$/DNA NSs (d–g) in 0.01 M PBS by stepping the potential from 0.92 to −1.80 (d), 0.69 to −1.80 (e), 0.92 to −1.45 (f) and 0.69 to −1.45 (g) at a frequency of 1 s. The blue curves indicate the applied potential. The photomultiplier tube voltage (PMT) for ECL measurements was biased at 750 V.

respectively, confirming that the measured heights of streptavidin in this study are consistent with prior reports.[29] In addition, we also demonstrate that the QDs were assembled onto the DNA nanosheets by laser confocal scanning microscopy. An organic fluorophore with red emission (Cy5; λ_{em} = 648 nm), was used to modify a DNA strand in the C tile of the DNA nanosheet. The 2D arrays containing both Cy5 and SA-$CsPbBr_3$ QDs with green emission (λ_{em} = 516 nm) were imaged through fluorescence imaging (Figure 1e). This imaging process revealed that the red Cy5 and the green QDs were colocalized on the DNA array further confirming that the QDs are successfully organized onto the DNA nanosheets.

X-ray photoelectron spectroscopy (XPS) and X-ray diffraction patterns (XRD) were employed to examine the states and crystalline structures of $CsPbBr_3$/DNA NSs. The XPS survey spectra of SA-$CsPbBr_3$ and $CsPbBr_3$/DNA NSs revealed the presence of elements C, N, O, Pd, Cs, and Br (Figure S6). High-resolution XPS spectra showed two peaks corresponding to Pb $4f_{7/2}$ and Pb $4f_{5/2}$ at 138.2 and 143.2 eV for $CsPbBr_3$/DNA NSs, and 138.0 and 142.95 eV for $CsPbBr_3$, respectively (Figure 1g). Similarly, Br $3d_{5/2}$ and Br $3d_{3/2}$ levels appeared at binding energies of 68.15 and 69.1 eV for $CsPbBr_3$/DNA NSs, compared to 67.95 and 69.0 eV for $CsPbBr_3$ QDs (Figure 1f). The observed shifts of approximately 0.2 eV in the binding energies of Pb 4f and Br 3d peaks after assembly suggest that charge transfer occurs between the $CsPbBr_3$ QDs and the DNA nanosheets.[30,31] The XRD pattern of $CsPbBr_3$/DNA NSs remains in the same cubic phase as that of monodisperse $CsPbBr_3$ QDs (PDF#54-0752).[32] Figure 1h shows that $CsPbBr_3$/DNA NSs has good crystallinity and high purity, and it is mainly oriented along the (110) crystal plane.

Effect of DNA Nanosheets on ECL Properties of $CsPbBr_3$. The effect of DNA nanosheets as a template for inducing $CsPbBr_3$ on electrochemiluminescence (ECL) properties was investigated for the first time. As shown in Figure 2a, a pronounced annihilation ECL signal was observed for the glassy carbon electrode (GCE) modified with $CsPbBr_3$/DNA nanosheets ($CsPbBr_3$/DNA NSs/GCE) when scanning between 0 V and −2.2 V. In contrast, no ECL signal was detected in the bare GCE, and a relatively low signal was detected in the $CsPbBr_3$-modified GCE ($CsPbBr_3$/GCE) and the SA-$CsPbBr_3$-modified GCE (SA-$CsPbBr_3$/GCE). The ECL intensity increased by 2.5-fold after assembling the QDs onto the DNA nanosheets, highlighting the significant impact of DNA nanosheet integration on the ECL performance. Additionally, electrochemical impedance spectroscopy (EIS) measurements revealed a decrease in charge transfer resistance (R_{ct}) from 355 Ω for the $CsPbBr_3$/GCE to 100 Ω for $CsPbBr_3$/DNA NSs (Figure 2b). This decrease in R_{ct} indicates that the presence of the DNA nanosheets accelerate electron transfer between $CsPbBr_3$ and the electrode surface, thereby increasing the ECL reaction rate and enhancing the light emission.[33,34]

The electrochemical behavior of $CsPbBr_3$/DNA NSs was further investigated using differential pulse voltammetry (DPV). As depicted in Figure 2c, the anodic scan starting from −2.20 V revealed two sequential oxidation reactions,[35] Ox1 and Ox2, with peak potentials at approximately 0.69 and 0.92 V, respectively. These reactions suggest that $CsPbBr_3$/DNA NSs can successively accept holes, leading to the formation of oxidized radicals with different charge states, such as $CsPbBr_3$ QDs^+ and $CsPbBr_3$ QDs^{2+}. A cathodic scan starting at 1.5 V revealed three irreversible reduction processes: Red1, Red2, and Red3. The peak potential of Red1, occurring between −0.30 V and −0.64 V, was similar for both the bare GCE and $CsPbBr_3$-modified GCE, indicating that this process

https://doi.org/10.1021/acssensors.5c02005
ACS Sens. 2025, 10, 6231−6240

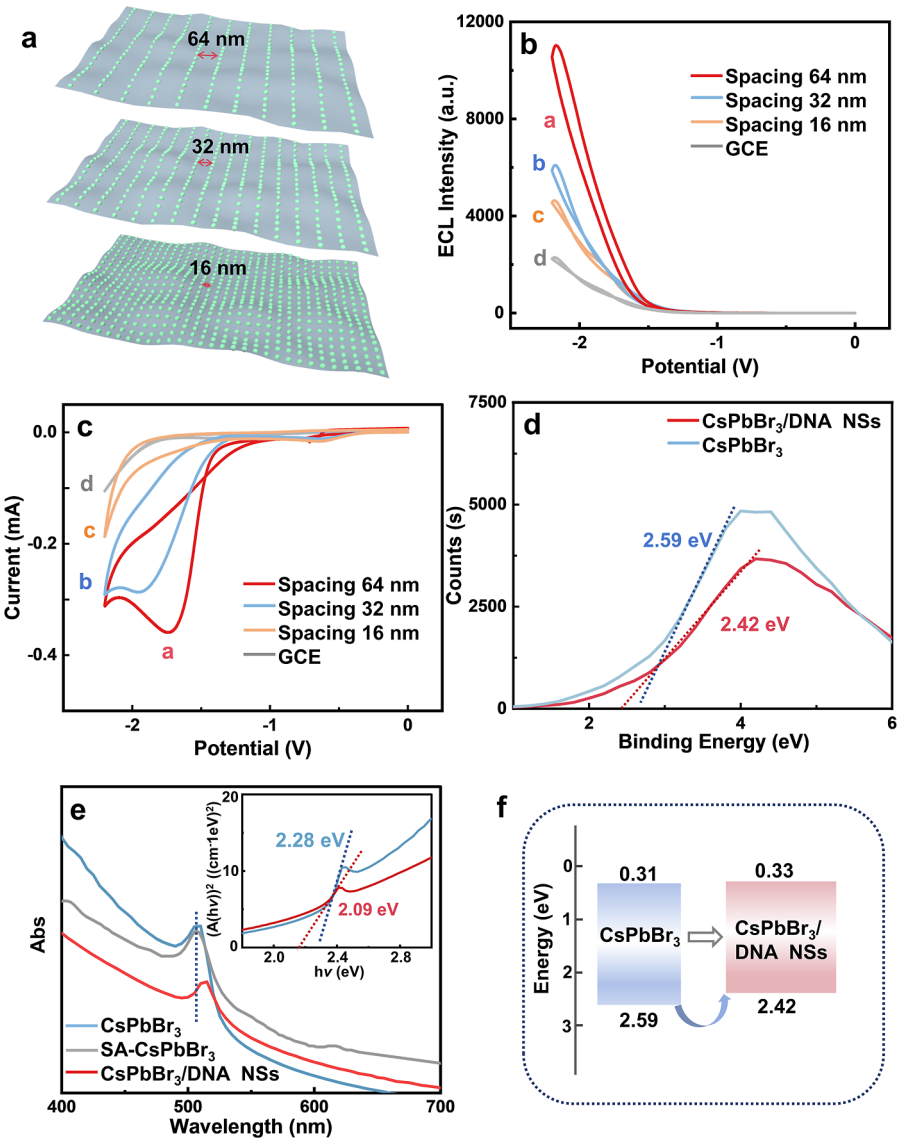

Figure 3. (a) Design drawings with different spacings. (b) ECL-potential curves and (c) CV of bare GCE and different spacings of $CsPbBr_3$/DNSs in 0.01 M PBS (pH = 7.4) containing 10 mM H_2O_2, (d) UPS (e) UV−vis absorption spectra and optical band gap derived from the $(Ah\nu)^2$ versus $h\nu$ plots of $CsPbBr_3$ QDs and $CsPbBr_3$/DNA NSs (inset). (f) Schematic illustration of the band structure.

is not associated with $CsPbBr_3$. In contrast, Red2, which rose slowly between −1.28 V and −1.58 V (peaking at −1.44 V), and Red3, which rose rapidly after −1.6 V, were attributed to the reduction of $CsPbBr_3$. These processes correspond to the formation of $CsPbBr_3^-$ and $CsPbBr_3^{2-}$ radicals, respectively, through the injection of electrons into the lowest unoccupied molecular orbital (LUMO) and the removal of electrons from the highest occupied molecular orbital (HOMO) of $CsPbBr_3$.[36,37] To further investigate the ECL properties, we employed an ECL transient technique. The annihilation ECL generated during electron transfer between anionic and cationic radicals[38] was examined by adjusting the $CsPbBr_3$/DNA NSs/GCE at different oxidation and reduction potentials. No ECL signal was observed when the potential was stepped to a positive value for 1 s, indicating that only holes were injected into the HOMO of $CsPbBr_3$. However, as depicted in Figures 2d−f, when the potential was switched from +0.92 V and +0.69 V to −1.8 V (or from +0.92 V and +0.69 V to −1.45 V), a distinct ECL signal was observed, confirming that the processes of Red2 and Red3 correspond to electron injection, while Ox1 and Ox2 are related to hole injection. The transient ECL spectra were nearly identical to the photoluminescence (PL) spectra of $CsPbBr_3$/DNA NSs, indicating that the excited states generated under different electrochemical conditions were consistent with those generated under optical excitation.

The DNA nanosheets serve as structural templates to effectively enhance the ECL properties of $CsPbBr_3$, primarily by improving the electron transfer between the QDs and the electrode surface. The results from DPV and ECL transient measurements provide a detailed understanding of the redox behavior and ECL mechanism of $CsPbBr_3$/DNA NSs, demonstrating their potential for high-performance ECL applications.

Effect of DNA Template Spacing on ECL Performance with Co-Reactant. To further explore the impact of DNA template vertical spacing on the ECL performance of $CsPbBr_3$, we designed three DNA nanosheets with varying intertemplate spacings (Figure 3a) and investigated their coreactive cathodic ECL using H_2O_2 as a coreactant. The successful synthesis of

https://doi.org/10.1021/acssensors.5c02005
ACS Sens. 2025, 10, 6231−6240

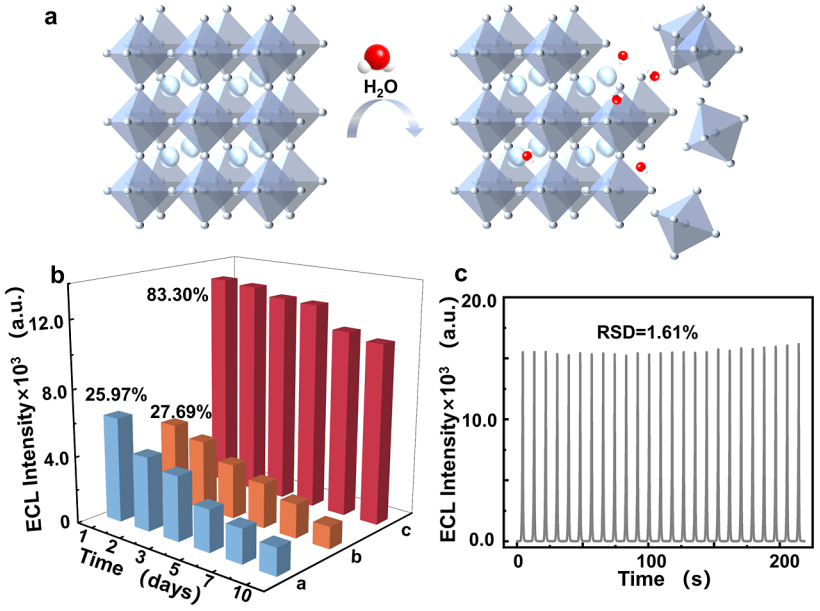

Figure 4. (a) Illustration of the structural collapse of $CsPbBr_3$ in aqueous environments. (b) ECL signalof $CsPbBr_3$ (a), SA-$CsPbBr_3$ (b) and $CsPbBr_3$/DNA NSs (c) in 0.01 M PBS (pH = 7.4) containing 10 mM H_2O_2 after a storage of 1, 2, 3, 5, 7, and 10 days at room temperature. (c) The stability of the developed $CsPbBr_3$/DNA NSs under 25 consecutive cyclic potential scans.

DNA nanosheets with micrometer-scale dimensions was confirmed by atomic force microscopy (AFM) (Figure S7). Following this, the DNA nanosheets were assembled with $CsPbBr_3$ QDs under the same experimental conditions. AFM images revealed that the nanocomponents self-assembled into parallel rows with inter-row separations of 32 and 16 nm (Figures S8−S11). The ECL performance of three $CsPbBr_3$/DNA NSs with different spacings was evaluated by potential-resolved ECL characterization. To eliminate potential background interference, we first measured the ECL response of DNA nanosheets alone (Figure S12), which exhibited only negligible background signals. As shown in Figure 3b, the ECL intensity of all three samples was enhanced in the presence of coreactants, compared to the bare GCE. This result confirms the critical role of DNA nanosheet-assisted self-assembly in improving the ECL emission. Notably, as the intertemplate spacing increased, the ECL intensity and ECL efficiency (vs $Ru(bpy)_3Cl_2/H_2O_2$ reference, see more details in the Supporting Information and Table S2) of $CsPbBr_3$/DNA NSs also increased, suggesting that larger template separations reduce the internal filtering effect,[39] thereby improving the emission of light. Cyclic voltammetry (CV) measurements were performed in 0.01 M phosphate-buffered saline (PBS) containing 10 mM H_2O_2 (Figure 3c). The data revealed that as the DNA template spacing increased, the redox potential shifted to more positive values, and the peak current increased, indicating an enhanced reduction process. On the bare GCE, H_2O_2 exhibited a strong reduction current with a peak at approximately −0.65 V, suggesting the formation of intermediate hydroxyl radicals (OH·) that oxidize $CsPbBr_3$ (R) to form $CsPbBr_3^+$ (R^+). For the $CsPbBr_3$/DNA NSs systems, a distinct reduction peak at −1.5 V was observed, demonstrating that electrons were successfully injected into the LUMO of $CsPbBr_3$, reducing the quantum dots to $CsPbBr_3^-$ (R^-). This further indicates that the interaction of H_2O_2 with $CsPbBr_3$/DNA NSs facilitates efficient electron transfer, which enhances the overall ECL response. Based on the above data, the following ECL mechanism can be proposed[10,38,40]

$$H_2O_2 + e \rightarrow OH^{\cdot} + OH^- \quad (1)$$

$$OH^{\cdot} + R \rightarrow R^+ + OH^- \quad (2)$$

$$R + e \rightarrow R^- \quad (3)$$

$$R^+ + R^- \rightarrow R^* \quad (4)$$

$$R^* \rightarrow R + h\nu \quad (5)$$

To further investigate the underlying electron transfer processes contributing to the enhanced ECL performance in the $CsPbBr_3$/DNA NSs system, we analyzed the valence band maximum (VBM) using valence band XPS (VB-XPS). The VBM values for $CsPbBr_3$/DNA NSs and $CsPbBr_3$ were estimated to be approximately 2.42 and 2.59 eV, respectively (Figure 3d). The red-shifted absorption spectrum of $CsPbBr_3$/DNA NSs (Figure 3e) compared to dispersed $CsPbBr_3$ indicates the presence of strongly interdot dipole interactions,[41,42] enhancing charge mobility and directional transport.[43] UV−vis absorption spectra and the Kubelka−Munk theory[44] were used to estimate the band gaps of $CsPbBr_3$/DNA NSs and $CsPbBr_3$, which were found to be approximately 2.09 and 2.28 eV, respectively. The reduction in the band gap and decrease in the HOMO energy level for $CsPbBr_3$/DNA NSs suggest that the self-assembly process promotes the separation of electron−hole pairs, which is beneficial for improving the ECL performance. Additionally, the fluorescence lifetime of $CsPbBr_3$/DNA NSs was measured (Figure S13), revealing an average value of 2.86 μs, which is shorter than the fluorescence lifetime of $CsPbBr_3$ (4.95 μs). This shorter lifetime is attributed to the nonradiative recombination pathways generated by the interaction between $CsPbBr_3$ QDs and DNA nanosheets, further supporting the enhancement of electron transfer.

The results demonstrate that DNA nanosheet template vertical spacing plays a crucial role in enhancing the ECL performance of $CsPbBr_3$. By increasing the intertemplate spacing, the efficiency of electron transfer is improved, leading to a stronger ECL signal.

https://doi.org/10.1021/acssensors.5c02005
ACS Sens. 2025, 10, 6231−6240

Scheme 2. Schematic Diagram of miRNA-221 Detection Mechanism Based on $CsPbBr_3$/DNA NSs

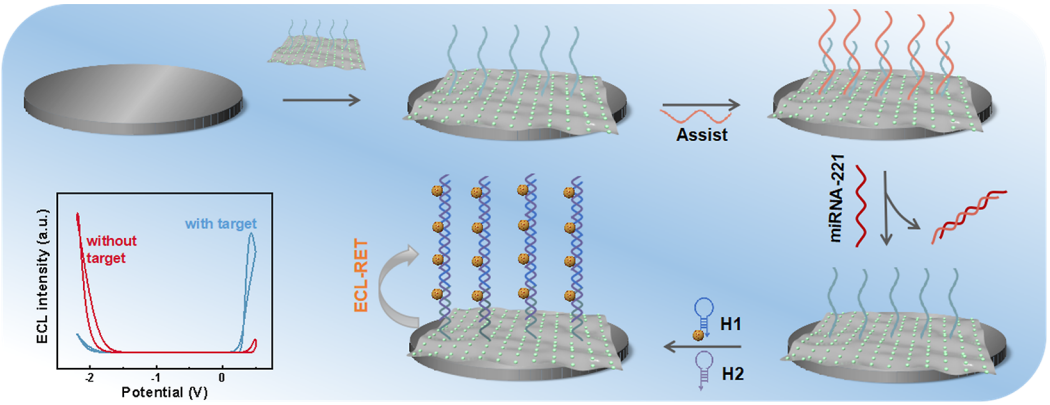

Stability of $CsPbBr_3$/DNA NSs. $CsPbBr_3$ QDs exhibit pronounced aggregation and rapid hydrolysis in aqueous environments, leading to accelerated structural collapse (Figure 4a). However, the self-assembly of $CsPbBr_3$ onto DNA nanosheets effectively mitigates this issue, ensuring the stability of the QDs in water. After 10 days of storage in pure water, $CsPbBr_3$/DNA NSs retained 83.3% of their initial ECL intensity, while the ECL signal of monodisperse $CsPbBr_3$ without the DNA template protection decreased by more than 70% (Figure 4b). This stark contrast underscores the significant role of DNA nanosheets in enhancing the water stability of $CsPbBr_3$. Under the optimum conditions, a good and stable ECL response can be obtained, and the relative standard deviation (RSD) of the ECL response for 25 consecutive scans is 2.04% (Figure 4c). In addition, the ECL efficiency (Φ_{ECL}) of the passivated $CsPbBr_3$ can approach up to 65.5%, two times higher than that of the pristine ones (≈33.5%). The DNA template preserves the structural integrity and ECL activity of the perovskite quantum dots, may be attributed to the formation of superlattice structures and more compact binding of surface ligands,[45] making them more suitable for practical applications. This finding is particularly important in the context of biosensor applications, where the longevity and reproducibility of the sensor signal are paramount.

Development of ECL-RET Biosensor for miRNA Detection. MicroRNAs (miRNAs) are an emerging class of endogenous, noncoding, single-stranded RNA molecules that play critical roles in various biological processes, including cell differentiation, apoptosis, proliferation, migration, invasion, and carcinogenesis.[46] Due to their involvement in numerous diseases, miRNAs have shown great potential as diagnostic biomarkers.[47] Consequently, the detection of miRNAs using electrochemical biosensors has garnered increasing attention from researchers.

In this study, we developed a dual-potential electrochemiluminescence resonance energy transfer (ECL-RET) biosensor (Scheme 2), integrated with a hybridization chain reaction (HCR),[48,49] for the sensitive and selective detection of miRNA-221. The biosensor was designed based on the principle of base complementary pairing. The extended strand of DNA nanosheets hybridizes with an auxiliary molecule (Assist strand) to form double-stranded DNA with sticky ends. Upon introducing miRNA-221, the target miRNA hybridizes with the Assist strand, displacing the extended strand. This interaction initiates the HCR process, involving the initiator and a mixture of Hairpin H1 and H_2, which amplifies the signal by generating double-stranded DNA polymers with Pt NPs-luminol, enhancing the ECL response. To enable the ECL-RET mechanism, Pt NPs-luminol was synthesized by reducing $PtCl_6^-$ with a luminal-sodium citrate solution, as previously reported.[50] This method effectively immobilizes luminal on the surface of Pt nanoparticles. The synthesized Pt NPs-luminol was characterized by TEM, revealing an average particle size of 2 nm (Figure S14a). The absorption peak of Pt NPs-luminol was observed at 360 nm, with a broader absorption range spanning 300 to 650 nm (Figure S14b). The ECL emission wavelengths of $CsPbBr_3$/DNA NSs, ranging from 400 to 700 nm, overlap with the absorption range of Pt NPs-luminol. This overlap facilitates ECL-RET between $CsPbBr_3$ and Pt NPs, resulting in the quenching of the cathodic ECL emission from $CsPbBr_3$.

The triggered hybridization chain reaction (HCR) was further characterized using polyacrylamide gel electrophoresis (PAGE). As shown in Figure S15, the band in lane 5 corresponds to a mixture of hairpins H1 and H_2, which shows no secondary structure formation, confirming the inactive state before the addition of the target miRNA. In lane 8, where no target miRNA-221 is present, the reaction does not proceed, and no amplified product is formed. However, in the presence of miRNA-221, the target miRNA hybridizes with the Assist strand, displacing the extended strand, and initiates the HCR process. This cycle of strand displacement and hybridization amplifies the signal by producing high-molecular-weight double-stranded DNA polymers with Pt NPs-luminol, significantly enhancing the ECL signal. To verify the stepwise-modified process of the electrode, cyclic voltammetry (CV) measurements were performed. The occurrence of the HCR led to a significant decrease in CV signals (Figure S16), which confirms the successful construction of the proposed biosensor.

The ECL-RET biosensor operates in a potential scanning range from −2.2 to 0.5 V, with hydrogen peroxide (H_2O_2) as the coreactant. During the scan, the ECL of $CsPbBr_3$/DNA NSs at −2.2 V and the ECL of luminol at 0.45 V were simultaneously induced. The introduction of Pt NPs-luminol quenched the cathodic ECL of $CsPbBr_3$/DNA NSs while significantly enhancing the anodic ECL of luminol. This ratiometric ECL-RET approach enables precise detection of miRNA-221, as it compensates for signal fluctuations and ensures reliability in complex environments.

https://doi.org/10.1021/acssensors.5c02005
ACS Sens. 2025, 10, 6231−6240

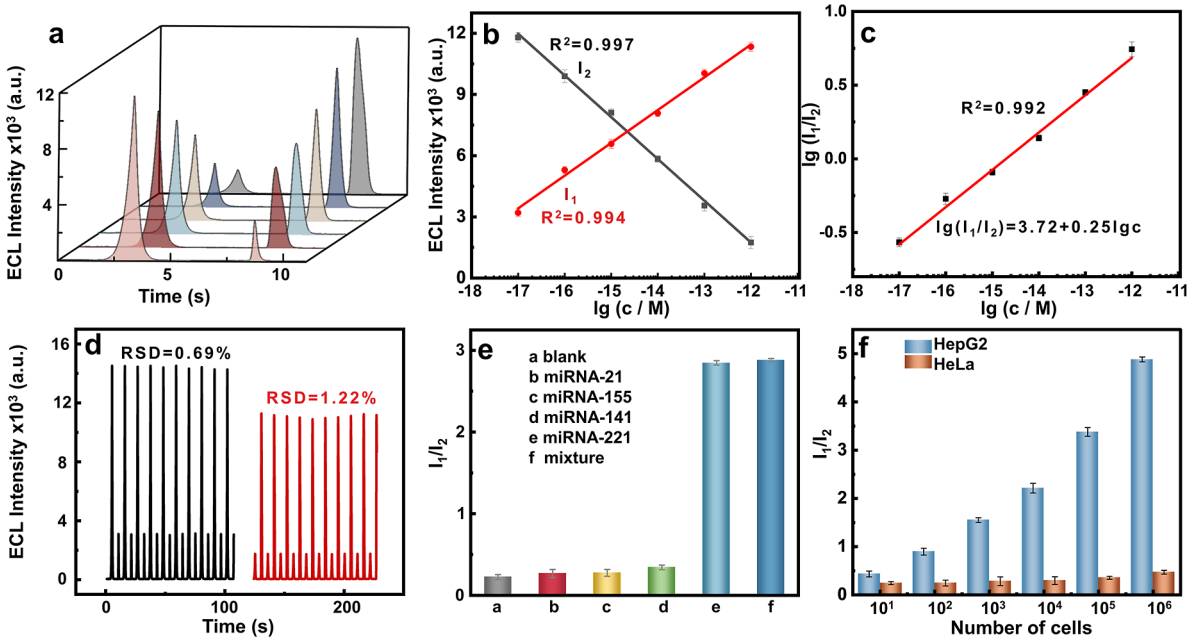

Figure 5. (a–c) Standard ECL responses of the $CsPbBr_3$/DNA NSs system upon addition of various concentrations of miRNA-221, (d) the stability of the developed $CsPbBr_3$/DNA NSs based sensing toward 0 and 1 pM under 10 consecutivecyclic potential scans. (e) Selectivity of the $CsPbBr_3$/DNA NSs based sensing assay for miRNA-221 detection over other interference, (f) ECL responses of ECL biosensor incubating the lysates of HeLa and HepG2 with different cells number.

The performance of the developed ECL-RET biosensor was further evaluated for detecting miRNA-221 in biological samples. First, we optimized the experimental conditions, including the concentration of Pt NPs and the reaction time of the HCR, to achieve the best ECL performance (Figure S17). The ECL intensity increased with Pt NPs concentration, reaching a maximum at 120 μM. The optimal HCR reaction time was found to be 3 h, during which the cathode-to-anode ECL intensity ratio increased. Under these optimized conditions, miRNA-221 detection was performed. As shown in Figure 5a, the ECL signal from $CsPbBr_3$/DNA NSs at −2.2 V decreased with increasing target miRNA concentration, while the ECL signal from Pt NPs-luminol at 0.45 V increased. The ECL intensity ratio (I_1/I_2) exhibited a strong linear correlation with miRNA-221 concentration, ranging from 10 aM to 10 pM (R^2 = 0.992), with a calculated limit of detection (LOD) of 6.05 aM (LOD = 3 Sb/m) (Figure 5c). Compared with other biosensors, the constructed biosensor exhibited a wider limit range and a lower detection limit (Table S3).

To assess the stability of biosensor, 10 consecutive cyclic potentiometric scans were performed with 0 M and 1 pM miRNA. As shown in Figure 5d, no significant change in ECL intensity was observed, demonstrating the high stability of the biosensor. The selectivity of the biosensor was also tested by introducing other microRNAs, including miRNA-21, miRNA-155, and miRNA-141. As shown in Figure 5e, the signal interference from these microRNAs was negligible, even when their concentration was 10 times higher than that of miRNA-221, indicating excellent selectivity for miRNA-221 detection.

Finally, the biosensor was tested in biological samples, including lysates from hepatocellular carcinoma (HepG2) and HeLa cells. As shown in Figure 5f, as the number of HepG2 cells increased from 10 to 10^5, the ECL ratio increased significantly, while the signal from HeLa cells remained relatively stable. These results suggest that miRNA-221 is overexpressed in HepG2 cells and underexpressed in HeLa cells, consistent with previously reported findings.[51] This confirms that the developed biosensing strategy is highly suitable for detecting miRNA-221 in cancer cells.

CONCLUSIONS

In conclusion, we present a novel strategy for enhancing the performance of $CsPbBr_3$ QDs by utilizing DNA nanosheets as templates to induce the self-assembly of $CsPbBr_3$ into long-range ordered close-packed superlattice. By combining biotin-modified staple chains with streptavidin-coated $CsPbBr_3$ QDs, we successfully organized the originally disordered nanocrystals into a stable and highly ordered superstructure in aqueous environments. This self-assembly approach enables tight packing of $CsPbBr_3$, facilitating efficient electron transport. Simultaneously addressing perovskite's aqueous instability while offering a generalizable nanomaterial design platform. A dual-potential ECL-RET biosensor was developed, which utilizes $CsPbBr_3$/DNA nanosheets for sensitive and selective detection of miRNA-221. The sensor exhibited exceptional stability and a low detection limit of 6.05 aM. This work not only provides a solution to the intrinsic instability of $CsPbBr_3$ QDs but also introduces a promising strategy for constructing high-performance ECL biosensors with broad applicability in disease detection and molecular diagnostics.

ASSOCIATED CONTENT

Supporting Information

The Supporting Information is available free of charge at https://pubs.acs.org/doi/10.1021/acssensors.5c02005.

Additional experimental details include reagents, apparatus, DNA oligonucleotide sequence information, synthesis and spectral testing of $CsPbBr_3$ QD and PtNPs-Luminol, AFM characterization, PAGE analysis of the sensing strategy, supplementary diagrams, supplementary tables and references (PDF)

https://doi.org/10.1021/acssensors.5c02005
ACS Sens. 2025, 10, 6231−6240

AUTHOR INFORMATION

Corresponding Authors

Pinyi Ma − *College of Chemistry, Jilin Province Research Center for Engineering and Technology of Spectral Analytical Instruments, Jilin University, Changchun 130012, China;* orcid.org/0000-0002-3230-4928; Email: mapinyi@jlu.edu.cn

Daqian Song − *College of Chemistry, Jilin Province Research Center for Engineering and Technology of Spectral Analytical Instruments, Jilin University, Changchun 130012, China;* orcid.org/0000-0002-4866-1292; Email: songdq@jlu.edu.cn

Authors

Yongli Wu − *College of Chemistry, Jilin Province Research Center for Engineering and Technology of Spectral Analytical Instruments, Jilin University, Changchun 130012, China*

Zhuoxin Ye − *College of Chemistry, Jilin Province Research Center for Engineering and Technology of Spectral Analytical Instruments, Jilin University, Changchun 130012, China*

Yuxuan Chen − *College of Chemistry, Jilin Province Research Center for Engineering and Technology of Spectral Analytical Instruments, Jilin University, Changchun 130012, China*

Yan Zhang − *College of Chemistry, Jilin Province Research Center for Engineering and Technology of Spectral Analytical Instruments, Jilin University, Changchun 130012, China*

Ruiyan Liu − *College of Chemistry, Jilin Province Research Center for Engineering and Technology of Spectral Analytical Instruments, Jilin University, Changchun 130012, China*

Complete contact information is available at: https://pubs.acs.org/10.1021/acssensors.5c02005

Notes

The authors declare no competing financial interest.

ACKNOWLEDGMENTS

This work was supported by the National Natural Science Foundation of China (22074052 and 22004046), the Science and Technology Developing Foundation of Jilin Province of China (20230101033JC), and the Jilin Provincial Department of Education Program for Enhancing Ph.D. Students' Scientific Research and Innovation Capabilities (JJKH20250064BS). The authors thank Prof. Chaoyong Yang (Shanghai Jiao Tong University) for helpful discussions.

REFERENCES

(1) Huang, H.; Susha, A. S.; Kershaw, S. V.; Hung, T. F.; Rogach, A. L. Control of Emission Color of High Quantum Yield $CH_3NH_3PbBr_3$ Perovskite Quantum Dots by Precipitation Temperature. *Adv. Sci.* **2015**, *2*, 1500194.

(2) Weidman, M. C.; Seitz, M.; Stranks, S. D.; Tisdale, W. A. Highly Tunable Colloidal Perovskite Nanoplatelets through Variable Cation, Metal, and Halide Composition. *ACS Nano* **2016**, *10*, 7830−7839.

(3) Lee, S.; Choi, M.-J.; Sharma, G.; Biondi, M.; Chen, B.; Baek, S.-W.; Najarian, A. M.; Vafaie, M.; Wicks, J.; Sagar, L. K.; Hoogland, S.; de Arquer, F. P. G.; Voznyy, O.; Sargent, E. H. Orthogonal Colloidal Quantum Dot Inks Enable Efficient Multilayer Optoelectronic Devices. *Nat. Commun.* **2020**, *11*, 4814.

(4) Peighambardoust, N. S.; Sadeghi, E.; Aydemir, U. Lead Halide Perovskite Quantum Dots for Photovoltaics and Photocatalysis: A Review. *ACS Appl. Nano Mater.* **2022**, *5*, 14092−14132.

(5) Cardenas-Morcoso, D.; Gualdrón-Reyes, A. F.; Ferreira Vitoreti, A. B.; García-Tecedor, M.; Yoon, S. J.; Solis de la Fuente, M.; Mora-Seró, I.; Gimenez, S. Photocatalytic and Photoelectrochemical Degradation of Organic Compounds with All-Inorganic Metal Halide Perovskite Quantum Dots. *J. Phys. Chem. Lett.* **2019**, *10*, 630−636.

(6) Meng, J.; Lan, Z.; Abdellah, M.; Yang, B.; Mossin, S.; Liang, M.; Naumova, M.; Shi, Q.; Gutierrez Alvarez, S. L.; Liu, Y.; Lin, W.; Castelli, I. E.; Canton, S. E.; Pullerits, T.; Zheng, K. Modulating Charge-Carrier Dynamics in Mn-Doped All-Inorganic Halide Perovskite Quantum Dots through the Doping-Induced Deep Trap States. *J. Phys. Chem. Lett.* **2020**, *11*, 3705−3711.

(7) Bi, C.; Kershaw, S. V.; Rogach, A. L.; Tian, J. Improved Stability and Photodetector Performance of Cspbi3 Perovskite Quantum Dots by Ligand Exchange with Aminoethanethiol. *Adv. Funct. Mater.* **2019**, *29*, 1902446.

(8) Gao, F.; Yang, W.; Liu, X.; Li, Y.; Liu, W.; Xu, H.; Liu, Y. Highly Stable and Luminescent Silica-Coated Perovskite Quantum Dots at Nanoscale-Particle Level Via Nonpolar Solvent Synthesis. *Chem. Eng. J.* **2021**, *407*, 128001.

(9) Cho, S.; Yun, S. H. Poly(Catecholamine) Coated $Cspbbr_3$ Perovskite Microlasers: Lasing in Water and Biofunctionalization. *Adv. Funct. Mater.* **2021**, *31*, 2101902.

(10) Tan, X.; Zhang, B.; Zou, G. Electrochemistry and Electrochemiluminescence of Organometal Halide Perovskite Nanocrystals in Aqueous Medium. *J. Am. Chem. Soc.* **2017**, *139*, 8772−8776.

(11) Wang, C.; Shim, M.; Guyot-Sionnest, P. Electrochromic Nanocrystal Quantum Dots. *Science* **2001**, *291*, 2390−2392.

(12) Quan, L. N.; Yuan, M.; Comin, R.; Voznyy, O.; Beauregard, E. M.; Hoogland, S.; Buin, A.; Kirmani, A. R.; Zhao, K.; Amassian, A.; Kim, D. H.; Sargent, E. H. Ligand-Stabilized Reduced-Dimensionality Perovskites. *J. Am. Chem. Soc.* **2016**, *138*, 2649−2655.

(13) Teunis, M. B.; Jana, A.; Dutta, P.; Johnson, M. A.; Mandal, M.; Muhoberac, B. B.; Sardar, R. Mesoscale Growth and Assembly of Bright Luminescent Organolead Halide Perovskite Quantum Wires. *Chem. Mater.* **2016**, *28*, 5043−5054.

(14) Lena, A. M.; Yamauchi, M.; Murakami, H.; Kubo, N.; Masuo, S.; Matsuo, K.; Hayashi, H.; Aratani, N.; Yamada, H. Orderly Arranged Cubic Quantum Dots Along Supramolecular Templates of Naphthalenediimide Aggregates. *Angew. Chem., Int. Ed.* **2025**, *64*, No. e202423912.

(15) Vila-Liarte, D.; Feil, M. W.; Manzi, A.; Garcia-Pomar, J. L.; Huang, H.; Döblinger, M.; Liz-Marzán, L. M.; Feldmann, J.; Polavarapu, L.; Mihi, A. Templated-Assembly of Cspbbr3 Perovskite Nanocrystals into 2d Photonic Supercrystals with Amplified Spontaneous Emission. *Angew. Chem., Int. Ed.* **2020**, *59*, 17750−17756.

(16) Wei, W.-J.; Jiang, X.-X.; Dong, L.-Y.; Liu, W.-W.; Han, X.-B.; Qin, Y.; Li, K.; Li, W.; Lin, Z.-S.; Bu, X.-H.; Lu, P.-X. Regulating Second-Harmonic Generation by Van Der Waals Interactions in Two-Dimensional Lead Halide Perovskite Nanosheets. *J. Am. Chem. Soc.* **2019**, *141*, 9134−9139.

(17) Pramanik, A.; Patibandla, S.; Gao, Y.; Gates, K.; Ray, P. C. Water Triggered Synthesis of Highly Stable and Biocompatible 1d Nanowire, 2D Nanoplatelet, and 3D Nanocube $Cspbbr_3$ Perovskites for Multicolor Two-Photon Cell Imaging. *JACS Au* **2021**, *1*, 53−65.

(18) Yang, Y.; Lee, J. T.; Liyanage, T.; Sardar, R. Flexible Polymer-Assisted Mesoscale Self-Assembly of Colloidal $CsPbBr_3$ Perovskite Nanocrystals into Higher Order Superstructures with Strong Inter-Nanocrystal Electronic Coupling. *J. Am. Chem. Soc.* **2019**, *141*, 1526−1536.

(19) Li, X.; Wang, J.; Baptist, A.; Wu, W.; Heuer-Jungemann, A.; Zhang, T. Crystalline Assemblies of DNA Nanostructures and Their Functional Properties. *Angew. Chem., Int. Ed.* **2025**, *64*, No. e202416948.

(20) Lu, L.-X.; Bharathi, M. S.; Zhang, Y.-W. Self-Assembly of Ordered Epitaxial Nanostructures on Polygonal Nanowires. *Nano Lett.* **2013**, *13*, 538−542.

(21) Talapin, D. V.; Murray, C. B. Pbse Nanocrystal Solids for N- and P-Channel Thin Film Field-Effect Transistors. *Science* **2005**, *310*, 86−89.

(22) Baumgardner, W. J.; Whitham, K.; Hanrath, T. Confined-but-Connected Quantum Solids Via Controlled Ligand Displacement. *Nano Lett.* **2013**, *13*, 3225−3231.
(23) Lingley, Z.; Lu, S.; Madhukar, A. The Dynamics of Energy and Charge Transfer in Lead Sulfide Quantum Dot Solids. *J. Appl. Phys.* **2014**, *115*, 084302.
(24) Sharifi, T.; Gracia-Espino, E.; Reza Barzegar, H.; Jia, X.; Nitze, F.; Hu, G.; Nordblad, P.; Tai, C.-W.; Wågberg, T. Formation of Nitrogen-Doped Graphene Nanoscrolls by Adsorption of Magnetic Γ-Fe_2O_3 Nanoparticles. *Nat. Commun.* **2013**, *4*, 2319.
(25) Akkerman, Q. A.; Rainò, G.; Kovalenko, M. V.; Manna, L. Genesis, Challenges and Opportunities for Colloidal Lead Halide Perovskite Nanocrystals. *Nat. Mater.* **2018**, *17*, 394−405.
(26) Loiudice, A.; Saris, S.; Oveisi, E.; Alexander, D. T. L.; Buonsanti, R. $CsPbBr_3$ QD/AlO Inorganic Nanocomposites with Exceptional Stability in Water, Light, and Heat. *Angew. Chem., Int. Ed.* **2017**, *56*, 10696−10701.
(27) Sharma, J.; Ke, Y.; Lin, C.; Chhabra, R.; Wang, Q.; Nangreave, J.; Liu, Y.; Yan, H. DNA-Tile-Directed Self-Assembly of Quantum Dots into Two-Dimensional Nanopatterns. *Angew. Chem., Int. Ed.* **2008**, *47*, 5157−5159.
(28) Li, X.; Wu, Y.; Zhang, S.; Cai, B.; Gu, Y.; Song, J.; Zeng, H. $CsPbX_3$ Quantum Dots for Lighting and Displays: Room-Temperature Synthesis, Photoluminescence Superiorities, Underlying Origins and White Light-Emitting Diodes. *Adv. Funct. Mater.* **2016**, *26*, 2435−2445.
(29) Weisenhorn, A. L.; Schmitt, F. J.; Knoll, W.; Hansma, P. K. Streptavidin Binding Observed with an Atomic Force Microscope. *Ultramicroscopy* **1992**, *42*−*44*, 1125−1132.
(30) Zhu, M.; Kim, S.; Mao, L.; Fujitsuka, M.; Zhang, J.; Wang, X.; Majima, T. Metal-Free Photocatalyst for H_2 Evolution in Visible to near-Infrared Region: Black Phosphorus/Graphitic Carbon Nitride. *J. Am. Chem. Soc.* **2017**, *139*, 13234−13242.
(31) Zhang, Y.; Tian, Y.; Chen, W.; Zhou, M.; Ou, S.; Liu, Y. Construction of a Bismuthene/$CsPbBr_3$ Quantum Dot S-Scheme Heterojunction and Enhanced Photocatalytic CO_2 Reduction. *J. Phys. Chem. C* **2022**, *126*, 3087−3097.
(32) Li, L.; Zhang, Z.; Chen, Y.; Xu, Q.; Zhang, J.-R.; Chen, Z.; Chen, Y.; Zhu, J.-J. Sustainable and Self-Enhanced Electrochemiluminescent Ternary Suprastructures Derived from Cspbbr3 Perovskite Quantum Dots. *Adv. Funct. Mater.* **2019**, *29*, 1902533.
(33) Han, Z.; Yang, Z.; Sun, H.; Xu, Y.; Ma, X.; Shan, D.; Chen, J.; Huo, S.; Zhang, Z.; Du, P.; Lu, X. Electrochemiluminescence Platforms Based on Small Water-Insoluble Organic Molecules for Ultrasensitive Aqueous-Phase Detection. *Angew. Chem., Int. Ed.* **2019**, *58*, 5915−5919.
(34) Ouyang, X.; Wu, Y.; Guo, L.; Li, L.; Zhou, M.; Li, X.; Liu, T.; Ding, Y.; Bu, H.; Xie, G.; Shen, J.; Fan, C.; Wang, L. Self-Assembly Induced Enhanced Electrochemiluminescence of Copper Nanoclusters Using DNA Nanoribbon Templates. *Angew. Chem., Int. Ed.* **2023**, *62*, No. e202300893.
(35) Sun, Q.; Ning, Z.; Yang, E.; Yin, F.; Wu, G.; Zhang, Y.; Shen, Y. Ligand-Induced Assembly of Copper Nanoclusters with Enhanced Electrochemical Excitation and Radiative Transition for Electrochemiluminescence. *Angew. Chem., Int. Ed.* **2023**, *62*, No. e202312053.
(36) Wei, X.; Chu, K.; Adsetts, J. R.; Li, H.; Kang, X.; Ding, Z.; Zhu, M. Nanocluster Transformation Induced by Sbf6− Anions toward Boosting Photochemical Activities. *J. Am. Chem. Soc.* **2022**, *144*, 20421−20433.
(37) Kang, X.; Li, Y.; Zhu, M.; Jin, R. Atomically Precise Alloy Nanoclusters: Syntheses, Structures, and Properties. *Chem. Soc. Rev.* **2020**, *49*, 6443−6514.
(38) Ding, Z.; Quinn, B. M.; Haram, S. K.; Pell, L. E.; Korgel, B. A.; Bard, A. J. Electrochemistry and Electrogenerated Chemiluminescence from Silicon Nanocrystal Quantum Dots. *Science* **2002**, *296*, 1293−1297.
(39) Jin, E.; Li, J.; Geng, K.; Jiang, Q.; Xu, H.; Xu, Q.; Jiang, D. Designed Synthesis of Stable Light-Emitting Two-Dimensional SP2 Carbon-Conjugated Covalent Organic Frameworks. *Nat. Commun.* **2018**, *9*, 4143.
(40) Peng, H.; Wu, W.; Huang, Z.; Xu, L.; Sheng, Y.; Deng, H.; Xia, X.; Chen, W. Cathodic Electrochemiluminescence Performance of All-Inorganic Perovskite $CsPbBr_3$ Nanocrystals in an Aqueous Medium. *Electrochem. Commun.* **2020**, *111*, 106667.
(41) Koole, R.; Liljeroth, P.; de Mello Donegá, C.; Vanmaekelbergh, D.; Meijerink, A. Electronic Coupling and Exciton Energy Transfer in Cdte Quantum-Dot Molecules. *J. Am. Chem. Soc.* **2006**, *128*, 10436−10441.
(42) Boev, V. I.; Filonovich, S. A.; Vasilevskiy, M. I.; Silva, C. J.; Gomes, M. J. M.; Talapin, D. V.; Rogach, A. L. Dipole−Dipole Interaction Effect on the Optical Response of Quantum Dot Ensembles. *Phys. B* **2003**, *338*, 347−352.
(43) Baranov, A. V.; Ushakova, E. V.; Golubkov, V. V.; Litvin, A. P.; Parfenov, P. S.; Fedorov, A. V.; Berwick, K. Self-Organization of Colloidal PbS Quantum Dots into Highly Ordered Superlattices. *Langmuir* **2015**, *31*, 506−513.
(44) Wang, Y.; Liu, X.; Liu, J.; Han, B.; Hu, X.; Yang, F.; Xu, Z.; Li, Y.; Jia, S.; Li, Z.; Zhao, Y. Carbon Quantum Dot Implanted Graphite Carbon Nitride Nanotubes: Excellent Charge Separation and Enhanced Photocatalytic Hydrogen Evolution. *Angew. Chem., Int. Ed.* **2018**, *57*, 5765−5771.
(45) Smock, S. R.; Williams, T. J.; Brutchey, R. L. Quantifying the Thermodynamics of Ligand Binding to $CsPbBr_3$ Quantum Dots. *Angew. Chem., Int. Ed.* **2018**, *57*, 11711−11715.
(46) de Ronde, M. W. J.; Ruijter, J. M.; Moerland, P. D.; Creemers, E. E.; Pinto-Sietsma, S.-J. Study Design and Qpcr Data Analysis Guidelines for Reliable Circulating Mirna Biomarker Experiments: A Review. *Clin. Chem.* **2018**, *64*, 1308−1318.
(47) Nasiri Khonsari, Y.; Sun, S. Recent Trends in Electrochemiluminescence Aptasensors and Their Applications. *Chem. Commun.* **2017**, *53*, 9042−9054.
(48) Huang, J.; Wu, Y.; Chen, Y.; Zhu, Z.; Yang, X.; Yang, C. J.; Wang, K.; Tan, W. Pyrene-Excimer Probes Based on the Hybridization Chain Reaction for the Detection of Nucleic Acids in Complex Biological Fluids. *Angew. Chem., Int. Ed.* **2011**, *50*, 401−404.
(49) Li, C.; Lu, W.; Zhou, X.; Pang, M.; Luo, X. Visible-Light Driven Photoelectrochemical Platform Based on the Cyclometalated Iridium-(Iii) Complex with Coumarin 6 for Detection of Microrna. *Anal. Chem.* **2018**, *90*, 14239−14246.
(50) Zhang, H.-R.; Xu, J.-J.; Chen, H.-Y. Electrochemiluminescence Ratiometry: A New Approach to DNA Biosensing. *Anal. Chem.* **2013**, *85*, 5321−5325.
(51) Rong, M.; Chen, G.; Dang, Y. Increased Mir-221 Expression in Hepatocellular Carcinoma Tissues and Its Role in Enhancing Cell Growth and Inhibiting Apoptosis in Vitro. *BMC Cancer* **2013**, *13*, 21.

https://doi.org/10.1021/acssensors.5c02005
ACS Sens. 2025, 10, 6231−6240